in HS macromolecular structures associated with solution chemistry may be caused by the protonation, deprotonation, and metal complexation of HS functional groups. The noted differences between the macromolecular structures of HSs of different origin are a reflection of the low solubility, higher aromatic C content, and the low carboxyl content of soil materials relative to fluvial humics (*1–6*). These results indicate that HSs exhibit more than one type of macromolecular structure in aqueous solutions, as opposed to the notion that HSs form rings in acidic and high ionic strength solutions and elongated structures in alkaline solutions (*12*). Globular and net-, ring-, and sheetlike structures have also been reported for soil HSs on substrate surfaces, such as mica and electron microscope sample substrates (*13–18*). As shown in this study, macromolecular structures of HSs associated with mineral oxides may not necessarily represent those in solution.

Changes in the HS macromolecular structures can modify the exposed surface area and alter the functional group chemistry of HSs, such as protonation and cation complexation. The common occurrence of HSs in more than one type of structure under pH conditions typical to the natural systems can substantially affect the biogeochemical processes in soils and sediments and the properties of aquatic colloids (*1–5*). In acidic soils and sediments with high C content, HSs can form dense structures with a low ratio of surface area to volume, in comparison to that of the alkaline soils. These structures can restrict the accessibility of micropores of HS aggregates to microorganisms and oxygen diffusion and thus inhibit the oxidation of organic matter and facilitate the stabilization of organic C by soils (*3–5*). Although fresh organic matter inputs are typically low in alkaline soils worldwide, the occurrence of HSs as open structures with high surface area under these conditions may also aggravate the C retention by alkaline soils (*4, 19*). For the same reasons, differences in HS macromolecular structures can also modify the intensity and rates of sorption, desorption, and biotransformation of contaminants (such as pesticides and chlorinated solvents) in soils and sediments (*3, 5*). Differences in the macromolecular structures of mineral-complexed HSs (with respect to size and C content) affect the properties of organomineral aggregates and control the chemistry of C retained by minerals in a soil profile, thus influencing the soil and sediment solution chemistry and their biogeochemical processes. These chemical and structural interactions of HSs can be explored directly with the high-resolution in situ x-ray spectromicroscopy methods.

References and Notes

1. F. J. Stevenson, *Humus Chemistry* (Wiley, New York, 1994).
2. D. S. Orlov, *Humic Substances of Soils and General Theory of Humification* (Balkema, Brookfield, VT, 1995).
3. R. Schwarzenbach, P. M. Gschwend, D. M. Imboden, *Environmental Organic Chemistry* (Wiley, New York, 1993).
4. J. I. Hedges and J. M. Oades, *Org. Geochem.* **27**, 319 (1997).
5. P. M. Huang and M. Schnitzer, *Soil Sci. Soc. Am. Spec. Publ. 17* (1986).
6. M. Schnitzer, *Soil Sci.* **151**, 41 (1991).
7. R. C. Averett, J. A. Leenheer, D. M. McKnight, K. A. Thorn, *U.S. Geol. Surv. Water Supply Pap. 2373* (1995).
8. D. L. Spark, Ed., *Methods of Soil Analysis: Part 3, Chemical Methods* (Soil Science Society of America, Madison, WI, 1996).
9. Kaolinite and montmorillonite were obtained from the Clay Mineral Society, calcite was reagent grade, and goethite was prepared by titrating $FeCl_3$ solution. The solid concentration in the experiments varied between 1 and 5 g of mineral per liter.
10. In an x-ray microscope, the contrast of the sample comes from the photoelectric absorption of x-rays, and hence, element- and functional group–specific images can be obtained at high spectral resolution for organic molecules. This instrument uses zone-plate optics to illuminate the sample (~10-μm field) and to form an enlarged image on an x-ray charge-coupled device camera. The spatial resolution of the microscope is currently 43 nm, limited by the zone-plate optics. However, the Poisson noise slightly reduces the resolution for images taken above the oxygen K-edge (543 eV) because of absorption by water. In addition, the sample nature (for example, mineral versus microbe) also determines the attainable spatial resolution. For collecting images, liquid samples or soil pastes (5.0 μl) were placed between two Si_3N_4 windows (thickness, 100 nm), and this entire assembly was placed at the focal point of the zone plates. Small changes in the concentration of soluble species may occur in samples because of water evaporation losses during imaging. To prevent such changes, we collected images immediately after they were placed in the holder. The chemical conditions reported here represent samples in the initial stages. Typically, the x-ray exposure to the sample varied from a few seconds to 60 s. The natural organics did not show any visible damage or modifications under these exposure times or after several exposures. For more information on the x-ray microscope of LBNL, see work by W. Meyer-Ilse *et al.*, *Synchrotron Radiat. News* **8**, 29 (1995). Descriptions of x-ray spectromicroscopy are available in work by G. Schmahl *et al.*, *Optik* **93**, 95 (1993); J. Kirz, C. Jacobson, M. Howells, *Q. Rev. Biophys.* **28**, 33 (1995); and J. Thieme *et al.*, *X-ray Microscopy and Spectromicroscopy* (Springer, Berlin, 1998).
11. W. Stumm, *Chemistry of the Solid-Water Interfaces* (Wiley, New York, 1993).
12. K. Ghosh and M. Schnitzer, *Soil Sci.* **129**, 266 (1980).
13. Y. Chen and M. Schnitzer, *Soil Sci. Soc. Am. J.* **40**, 682 (1976).
14. I. L. Stevenson and M. Schnitzer, *Soil Sci.* **133**, 179 (1982).
15. J. Buffle *et al.*, *Environ. Sci. Technol.* **32**, 2887 (1998).
16. N. Senesi, F. R. Rizzi, P. Acquafredda, *Colloids Surf A* **127**, 57 (1997).
17. D. K. Namjesnik and P. A. Maurice, *Colloids Surf. A* **120**, 77 (1997).
18. P. A. Maurice and D. K. Namjesnik, *Environ. Sci. Technol.* **33**, 1538 (1999).
19. H. Jenny, *Factors of Soil Formation: A System of Quantitative Pedology* (McGraw-Hill, New York, 1941).

20. S.C.B.M. dedicates this paper in memory of his co-author, Werner Meyer-Ilse. The authors thank T. K. Tokunaga, S. M. Benson, G. E. Brown, G. Sposito, S. J. Traina, and P. Maurice for helpful discussions and reviews of the manuscript and A. Lucero for help with the image processing. The research is funded by the Laboratory Directed Research and Development program of LBNL and by the Basic Energy Sciences (Geosciences) program of the U.S. Department of Energy.

14 July 1999; accepted 12 October 1999

Origin of Magnetization Decay in Spin-Dependent Tunnel Junctions

Martha R. McCartney,[1]* Rafal E. Dunin-Borkowski,[1]† Michael R. Scheinfein,[2] David J. Smith,[1,2] Savas Gider,[3] Stuart S. P. Parkin[3]

Spin-dependent tunnel junctions based on magnetically hard and soft ferromagnetic layers separated by a thin insulating barrier have emerged as prime candidates for information storage. However, the observed instability of the magnetically hard reference layer, leading to magnetization decay during field cycling of the adjacent soft layer, is a serious concern for future device applications. Using Lorentz electron microscopy and micromagnetic simulations, the hard-layer decay was found to result from large fringing fields surrounding magnetic domain walls in the magnetically soft layer. The formation and motion of these walls causes statistical flipping of magnetic moments in randomly oriented grains of the hard layer, with a progressive trend toward disorder and eventual demagnetization.

The resurgence of interest in magnetic thin films has been driven by the discovery of large magnetoresistance (MR) effects in multilayered films (*1*–3), spin-valve structures (*4*), and tunnel junctions (*5*, *6*). Typically, spin-dependent magnetic tunnel junctions (MTJs) consist of ferromagnetic (FM) layers separated by a thin insulating barrier, which is most often alumina. When the magnetization directions of the FM layers are parallel, there is a high probability of electrons with like spins tunneling between layers, and the resistance (R) is low. Conversely, when the magnetization is antiparallel, the tunneling probability is low and R is high. Devices based on the MR effect, such as magnetic

random access memory (MRAM), take advantage of the large difference in R between the parallel and antiparallel states of the junction (*7*, *8*). The magnetization of the magnetically hard (reference) layer should remain fixed when the soft (free) layer is reversed. For recording applications, repeated switching of the soft layer should not affect the hard-layer magnetization, because the MTJ memory would effectively be erased if this occurred.

In studies involving field cycling of a spin-dependent MTJ, the magnetic moment of a hard $Co_{75}Pt_{12}Cr_{13}$ layer (coercive field, H_c, ~1600 Oe) decayed logarithmically as the adjacent soft Co layer was cycled through ±200 Oe, eventually becoming fully demagnetized (*9*). The MTJ magnetic stability depends on the soft-layer composition (a free layer of $Ni_{40}Fe_{60}$ was much more stable than Co), the hard-layer magnetic moment (doubling of thickness from 5 to 10 nm greatly delayed magnetization decay), and the alumina tunnel-barrier thickness. When coherent field rotation of the soft layer was used to achieve magnetization reversal, no decay was observed. Because field reversal normally proceeds by formation or motion of domain walls (or both), neither of which occurs during field rotation, it appears likely that domain walls in the soft layer might have been responsible for the decay (*9*). Because of this uncertainty surrounding the origin of the magnetization decay and because of its fundamental and technological importance, we have undertaken a comprehensive examination of representative MTJs using Lorentz electron microscopy (*10*) and micromagnetic simulations based on solutions to the Landau-Lifshitz-Gilbert (LLG) equations (*11*). Samples were prepared by means of magnetron sputtering onto thin (55-nm), electron-transparent, silicon nitride windows. The alumina barrier was formed by deposition of metallic Al, followed by in-situ plasma oxidation.

Comparing the same region of the CoPtCr/alumina/Co film at in-plane applied fields of zero (Fig. 1A) and −200 Oe (Fig. 1B), respectively, analysis of image features such as the high-contrast domain walls and the strong magnetization ripple leads to the conclusion that these must originate primarily from the Co soft layer (*12*). For example, the single-

[1]Center for Solid State Science, [2]Department of Physics and Astronomy, Arizona State University, Tempe, AZ 85287–1704, USA. [3]IBM Almaden Research Center, 650 Harry Road, San Jose, CA 95120–6099, USA.

*To whom correspondence should be addressed. E-mail: molly.mccartney@asu.edu.

†Present address: Department of Materials, University of Oxford, Parks Road, Oxford OX1 3PH, UK.

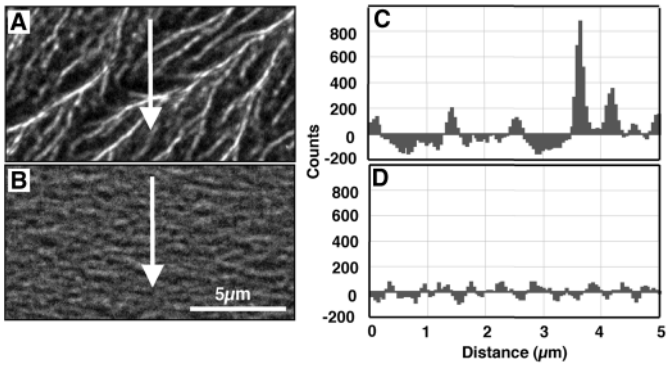

Fig. 1. Enlargements of Lorentz micrographs of a CoPtCr (15 nm)/alumina (1.4 nm)/Co (10 nm) film taken at (**A**) zero in-plane magnetic field and (**B**) ~−200 Oe. Corresponding line traces from the regions marked are shown in (**C**) and (**D**).

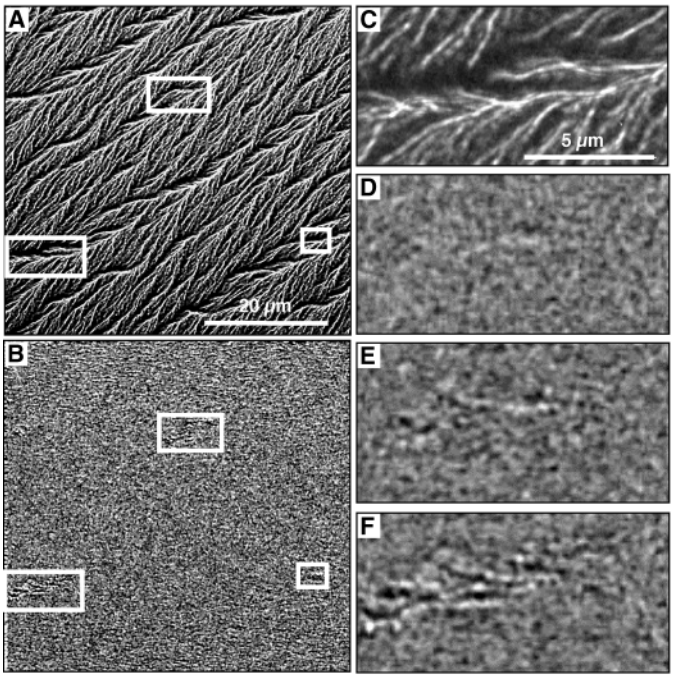

Fig. 2. Montage of Lorentz micrographs of CoPtCr alumina/Co MTJs during field cycling after initial magnetization of the hard layer with an in-plane field of ~10 kOe. (**A**) Zero in-plane field. Domain walls and ripple contrast are due primarily to the soft Co layer. (**B**) Difference image from same area as (A) between zero and 1000 cycles at an in-plane field of ~−200 Oe. (**C**) Enlargement from boxed area at bottom left of (A). (**D**) Difference image at −200 Oe showing the same region as in (C) after 5 cycles; (**E**) after 100 cycles; and (**F**) after 1000 cycles.

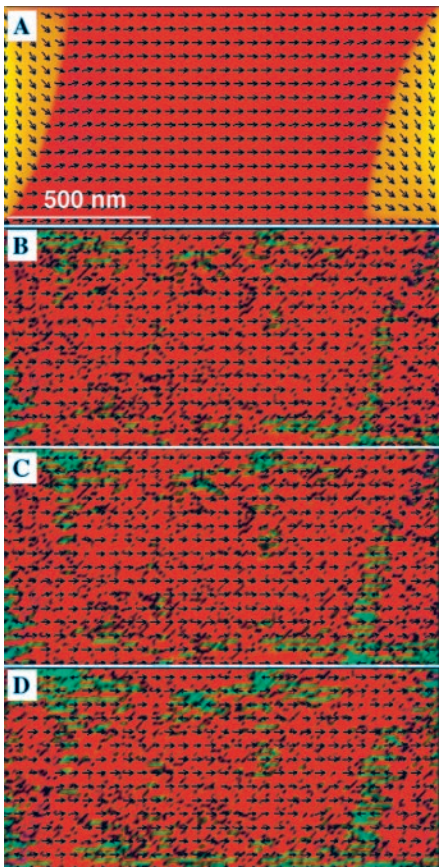

Fig. 3. Simulations of a CoPtCr/alumina/Co MTJ cell with dimensions of 1280 nm by 640 nm. Directions are indicated by arrows and by colors as follows: right, red; down, yellow; left, green; and up, blue. The color intensity reflects the magnitude of in-plane magnetization. The brightest colors have magnetization lying completely in-plane, with black being completely out-of-plane. (**A**) Equilibrium remanent S-state in the Co overlayer. The domain pattern is repeatedly cycled with an in-plane field of ±200 Oe. As domain walls in the Co overlayer move back and forth over the CoPtCr underlayer, regions of the latter are gradually flipped from having magnetization along the positive x direction (red) to lying along the negative x direction (green). Magnetization patterns in the CoPtCr underlayer are shown for 5, 9, and 20 cycles in (**B**) through (**D**), respectively. Evidence for progressive demagnetization is shown by the increase in number and size of the reversed (green) domains.

pixel line scan (Fig. 1C) shows high-contrast features on the order of 0.5 to 1.0 μm in length. When the Co layer is fully saturated (Fig. 1D), the image contrast has been reduced by approximately a factor of 3, with image periodicities in the 0.25-μm range.

When Lorentz micrographs of the CoPtCr/alumina/Co film taken at zero in-plane field (Fig. 2A) are compared with difference images (Fig. 2B) in which the regions marked have nonrandom (correlated) differences in contrast at an in-plane field of −200 Oe, it is clear that changes in the CoPtCr FM layer must have occurred between the time of the initial image and after cycling 1000 times. The succession of enlargements (Fig. 2, C through F) from the indicated area demonstrates the growth of a demagnetized region in the CoPtCr film as a result of repeated field cycling. It is especially important that there is close correlation between areas in the hard layer that have been demagnetized and positions where there are high-contrast domain walls in the soft Co layer. Some of these walls do not move freely through the Co as the field is reversed, but appear early in the hysteresis cycle and persist almost to the coercive field.

Micromagnetic simulations were used to further investigate the demagnetization processes (*11*). In these simulations for a CoPtCr/alumina/Co MTJ (Fig. 3), the model for the CoPtCr hard-layer material had random axis anisotropy (columnar structure) in a plane defined by the out-of-plane direction and one in-plane direction, and the transverse LLG cell dimensions were 10 nm by 10 nm. Representative values for the saturation magnetization and magnetocrystalline anisotropy of CoPtCr were used. The finite dimensions lead to boundary conditions that result in magnetization states with domain walls that are not randomly situated, thereby amplifying the demagnetization decay effect.

In the simulations, the field was cycled between ±200 Oe along the horizontal plane, as in the field cycling experiments. The equilibrium magnetization pattern of the Co layer (Fig. 3A) illustrates the stable configuration known as the S-state, which is characteristic of structures of this size (*13*). Corresponding domain patterns recorded after 5, 9, and 20 cycles (Fig. 3, B through D), respectively, show that the key result observed after field cycling is a progressive increase in the number and size of locally reversed (green) regions in the CoPtCr hard layer, primarily at soft-layer domain walls.

In thin magnetic films, the predominant type of boundary between adjacent magnetic domains is the Néel wall (*14*) (Fig. 4A). The horizontal and vertical components of the magnetic fringing field arising from the presence of a Néel wall in free layers of Co (Fig. 4B) were calculated as a function of out-of-plane distance from the wall. The individual curves indicate field strengths at distances of 2, 4, 6, 8, and 10 nm below the soft (free) layer. The in-plane stray field strengths directly below the Néel walls in Co and permalloy (in this case, $Ni_{80}Fe_{20}$) are summarized (Fig. 4C) as a function of distance. Because the average hard-layer coercivity is ~1600 Oe, the fringing field from a Co Néel wall could be large enough to reverse the magnetization within individual grains. Conversely, for a soft permalloy layer, the fringing field strength is much reduced and demagnetization will be much slower because only cells with specific anisotropy axes will be oriented so that demagnetization can proceed.

Demagnetization is more complicated in practice because of the random orientations of the magnetic easy axes of hard-layer grains. The initial, nearly saturated state of the hard layer is stabilized by the demagnetization fields of adjacent grains. When a domain wall in the soft layer moves over a grain, the stray field may be strong enough to rotate the magnetization and then reorient it. Once the magnetization direction is flipped, all neighboring grains experience the stray field from the reversed grain, thereby reducing the local field strength needed to flip subsequent grains. When the domain wall returns during the second half of the hysteresis cycle, some reversed grains may flip back. However, the probability of reversal occurring is proportional to the number of magnetization states present. Even though the field cycling process flips grains in both directions after each passage of a domain wall, the long-term average after many reversals approaches an equilibrium, with no net direction of the hard-layer magnetization. The entire hard-layer film will be effectively demagnetized even though the initial nucleation events are localized to regions in the soft layer where persistent domain walls are located. The presence of a vertical field in the microscope will reduce the flipping probability, but the trend toward magnetization decay will be unaltered.

Simulations of rotational hysteresis loops and of loops in which the hard layer was pinned with an exchange-coupled layer confirmed the experimental observations that there was no hard-layer demagnetization. For rotational loops, no domain walls were formed that could result in hard-layer demagnetization. For the exchange-coupled hard layer, the switching fields needed for reversal were raised above those that can be produced by stray fringing fields originating from Néel walls.

We have established that the magnetization decay observed in spin-dependent tunnel junctions can be attributed to the localized but very strong fringing fields associated with persistent magnetic domain walls. Random axis anisotropy between exchange-isolated grains in CoPtCr, a feature that gives this material desirable properties as a hard-disk medium, contribute to the mechanism of localized demagnetization. When the grains are coupled closely by an exchange mechanism, these demagnetization effects can be minimized or eliminated. The strength of these short-range interactions between adjacent magnetic layers is not generally well appreciated and should not be overlooked in future device applications.

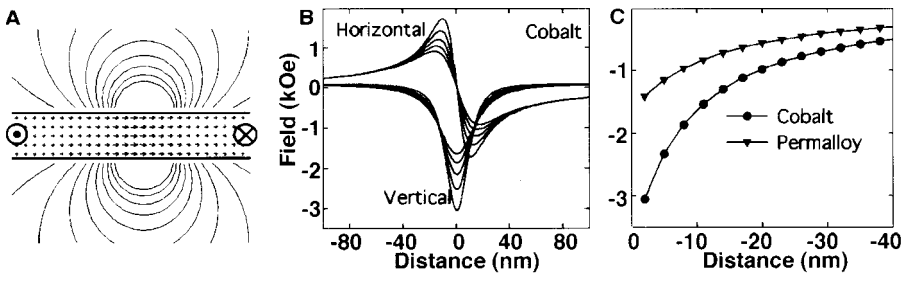

Fig. 4. (**A**) Schematic diagram of a Néel wall with fringing fields. (**B**) Position-dependent horizontal and vertical fringing fields for Co as a function of distance perpendicular to the wall for planes 2, 4, 6, 8, and 10 nm beneath the wall. (**C**) Field strength of the horizontal fringing field component directly beneath the Néel wall in Co and permalloy.

References and Notes

1. G. Binasch, R. Grünberg, F. Saurenbach, W. Zinn, *Phys. Rev. B* **39**, 4828 (1989).
2. M. N. Baibich *et al.*, *Phys. Rev Lett.* **61**, 2472 (1988).
3. S. S. P. Parkin, N. More, K. P. Roche, *Phys. Rev. Lett.* **64**, 2304 (1990).
4. B. Dieny *et al.*, *J. Appl. Phys.* **69**, 4772 (1991).
5. T. Miyazaki and N. J. Tezuka, *Magn. Magn. Mater.* **139**, L231 (1995).
6. J. S. Moodera, L. R. Kinder, T. M. Wong, R. Meservey, *Phys. Rev. Lett.* **74**, 3273 (1995).
7. W. J. Gallagher *et al.*, *J. Appl. Phys.* **81**, 3741 (1997).
8. S. S. P. Parkin *et al.*, *J. Appl. Phys.* **85**, 5828 (1999).
9. S. Gider, B.-U. Runge, A. C. Marley, S. S. P. Parkin, *Science* **281**, 797 (1998).
10. J. N. Chapman, *J. Phys. D* **17**, 623 (1984).
11. M. R. Scheinfein *et al.*, *Phys. Rev. B* **43**, 3395 (1991).
12. The magnetic microstructure was studied with a Philips CM200ST-FEG transmission electron microscope, equipped with a minilens for magnetic imaging, and a slow-scan charge-coupled device camera. The immersion objective lens provided a vertical field at the specimen of 825 Oe. The sample was repeatedly tilted

by ±14° with an automated goniometer to reverse the soft-layer magnetization, using the in-plane magnetic field of ±200 Oe (the hard CoPtCr film had been saturated by applying a 10-kOe in-plane field). Lorentz images were recorded at the sample tilt corresponding to −200 Oe when the soft FM layer was saturated and the remaining image contrast was due to residual magnetization ripple in the CoPtCr hard layer. All Lorentz images were recorded under identical conditions and were carefully aligned so that changes in contrast could be related to microstructural and micromagnetic features. Using image subtraction, contrast changes could be monitored, allowing the nucleation and growth of magnetic domains within the hard layer to be identified.

13. Y. Zheng and J.-G. Zhu, *J. Appl. Phys.* **81**, 5470 (1997).
14. A. Hubert, *Phys. Stat. Sol.* **38**, 699 (1970).

15. Partly supported by funding from the Advanced MRAM Project of the Defense Advanced Research Projects Agency. We acknowledge the use of facilities at the Center for High Resolution Electron Microscopy at Arizona State University. M.R.S. and S.S.P.P. thank P. Trouilloud of the IBM T.J. Watson Research Center for discussions that contributed substantially to this work, and we thank J. Speidell for supplying silicon nitride membranes.

19 July 1999; accepted 5 October 1999

Detection of Nonthermal Melting by Ultrafast X-ray Diffraction

C. W. Siders,[1]* A. Cavalleri,[1] K. Sokolowski-Tinten,[4] Cs. Tóth,[2] T. Guo,[1]† M. Kammler,[5] M. Horn von Hoegen,[6]‡ K. R. Wilson,[1] D. von der Linde,[4] C. P. J. Barty[3]

Using ultrafast, time-resolved, 1.54 angstrom x-ray diffraction, thermal and ultrafast nonthermal melting of germanium, involving passage through nonequilibrium extreme states of matter, was observed. Such ultrafast, optical-pump, x-ray diffraction probe measurements provide a way to study many other transient processes in physics, chemistry, and biology, including direct observation of the atomic motion by which many solid-state processes and chemical and biochemical reactions take place.

Many fundamental processes in nature, such as chemical and biochemical reactions and phase transitions, involve changes in the structure of matter: rearrangement of the constituent atoms and molecules. Such changes usually occur transiently on time scales that are comparable with the natural oscillation periods of atoms and molecules; that is, femtoseconds to picoseconds. Ultrashort-pulse visible lasers with such pulse widths have been used for more than two decades to optically pump and dynamically probe a wide array of atomic, molecular, solid-state, and plasma systems, including extreme states of matter normally found only in stellar or planetary interiors and experimentally accessible only by the rapid heating and inertial confinement made possible with ultrashort-pulse irradiation (*1*, *2*). In these experiments, however, the visible light used to probe the ensuing dynamics inherently cannot resolve atomic-scale features, and it interacts predominately with valence and free electrons and not with the deeper lying core electrons and nuclei that most directly indicate structure. Hard x-ray radiation, with wavelengths comparable with interatomic distances, is well suited to measure structure and atomic rearrangement and can measure structural dynamics in the interior of samples that are not transparent to ordinary light. Recently, subpicosecond sources of hard x-rays have been developed (*3*–*5*), making possible new classes of experiments in physics, chemistry, and biology (*4*, *6*–*9*). Visible-pump, x-ray diffraction probe experiments that measure the generation and propagation of coherent acoustic pulses in bulk gallium arsenide (GaAs) crystals have been reported (*7*). In those experiments, milli-angstrom changes in lattice spacing were measured with picosecond temporal resolution. Here we report on the observation, using time-resolved x-ray diffraction, of ultrafast nonthermal melting of short-pulse–irradiated germanium (Ge) (*10*).

In general, if a solid is heated to or above the melting temperature, nucleation of the liquid phase occurs around crystal defects or inclusions, usually at the surface itself, and the rate of phase change depends on the degree of superheating of the solid (*11*). In the case of laser irradiation of an absorbing crystalline semiconductor, incident optical energy is initially coupled to the carriers, which undergo band-to-band transitions. Intraband relaxation and nonradiative recombination cause delayed heating of the lattice (*12*), which exceeds the melting temperature within several picoseconds. After nucleation of the liquid phase at the surface, a thin liquid layer grows into the bulk of the material at a velocity depending on the degree of superheating of the interface but limited by the speed of sound. Typically, a layer a few tens of nanometers thick will melt in a few hundred picoseconds (*13*). This effect has been observed for irradiation with pulses longer than several picoseconds (*14*) and for near-threshold femtosecond pulses. In contrast, optical experiments using fluences twice the melting threshold or greater (*15*–*20*) exhibit a significantly faster, subpicosecond change of the linear optical properties at the surface, with reflectivities reaching, in a few hundred femtoseconds, values equal to that of the conventional liquid phase (*18*, *19*). In other experiments, a reduction in the second-harmonic-in-reflection signal, suggesting a subpicosecond loss of crystalline order at the very surface, was also seen (*15*, *16*, *18*). These observations indirectly indicate that an ultrafast solid-to-liquid phase transition occurs at the surface of the semiconductor on a time scale faster than carrier-lattice equilibration times. In order to directly observe the nonthermal loss of crystalline order both at the surface and in the bulk of the semiconductor lattice, we performed time-resolved, optical-pump, ultrafast x-ray diffraction probe experiments on laser-irradiated Ge.

Three samples, nominally 160 nm thick, were used, consisting of single-crystal Ge films grown by means of a novel surfactant-mediated growth technique (*21*) over large areas (7.6 cm in diameter) of single-crystal silicon substrates. These large-area layered samples allowed us to acquire data (*22*) using the same standards routinely used in ultrafast optical studies of nonreversible dynamics of solids: First, because the film thickness was smaller than both the optical and x-ray penetration lengths, the entire x-ray–probed depth was optically pumped; second, the large area permitted shot-by-shot sample translation at the 20-Hz laser repetition rate, thereby illuminating a fresh area of the sample on every shot.

Diffraction images were measured at different pump-probe time delays (Fig. 1). Because the diffracted x-rays emanated from a point source, the horizontal axis on the detector represents various diffraction angles, whereas the vertical axis gives the scattering position on the sample. The diffraction image taken at negative time delays (Fig. 1A) is identical to the unpumped case. The $K_{\alpha 1}$ and $K_{\alpha 2}$ spin-orbit-split lines of Cu are clearly

[1]Department of Chemistry and Biochemistry, [2]Institute for Nonlinear Science, [3]Department of Applied Mechanical/Engineering Sciences, University of California, San Diego, La Jolla, CA 92093–0339, USA. [4]Institut für Laser- und Plasmaphysik, Universität Essen, D-45117 Essen, Germany. [5]Institut für Halbleitertechnologie, [6]Institut für Festkörperphysik, Universität Hannover, D-30167 Hannover, Germany.

*To whom correspondence should be addressed. E-mail: csiders@ucsd.edu.
†Present address: Department of Chemistry, University of California, Davis, Davis, CA 95616, USA.
‡Present address: Institut für Laser- und Plasmaphysik, Universität Essen, D-45117 Essen, Germany.